Quantifying NO_x Emissions from U.S. Oil and Gas Production Regions Using TROPOMI NO_2

Dix, Barbara; Francoeur, Colby; Li, Meng; Serrano-Calvo, Raquel; Levelt, Pieternel F.; Veefkind, J. Pepijn; McDonald, Brian C.; De Gouw, Joost

DOI
10.1021/acsearthspacechem.1c00387

Publication date
2022

Document Version
Final published version

Published in
ACS Earth and Space Chemistry

ACS EARTH AND SPACE CHEMISTRY

http://pubs.acs.org/journal/aesccq

Article

Quantifying NO_x Emissions from U.S. Oil and Gas Production Regions Using TROPOMI NO_2

Barbara Dix,* Colby Francoeur, Meng Li, Raquel Serrano-Calvo, Pieternel F. Levelt, J. Pepijn Veefkind, Brian C. McDonald, and Joost de Gouw

Cite This: *ACS Earth Space Chem.* 2022, 6, 403−414

Read Online

ACCESS | Metrics & More | Article Recommendations | Supporting Information

ABSTRACT: The production of crude oil and natural gas is associated with emissions of air pollutants, such as nitrogen oxides (NO_x = NO + NO_2) and volatile organic compounds, which are precursors for the formation of ground-level ozone. Knowledge of these emissions is critical to the understanding and mitigation of local air quality. NO_x emissions from oil and gas production activities are not well described in commonly used emission inventories, and discrepancies of several factors have been found in the past. Here we present an easy and computationally efficient method to quantify NO_x emissions from satellite NO_2 observations that can be applied to evaluate common emission inventories and provide timely input for chemistry transport models. Using NO_2 columns from the TROPOspheric Monitoring Instrument (TROPOMI), we calculated annually averaged NO_x emissions from the divergence of NO_2 column fluxes for six oil and gas production regions in the United States. Derived NO_x emissions for the years 2018 to 2020 range between 4.8 and 81.1 t/day, and observed trends over time are consistent with changes in industrial activity. To evaluate the method, we compared our results with the fuel-based oil and gas NO_x inventory (FOG) and performed sensitivity studies using model output from the Weather Research Forecasting model with Chemistry (WRF-Chem). We found that annually averaged NO_x emissions from oil and gas production activities can in most cases be calculated within an uncertainty of 50%, while simultaneously derived emission maps show the spatial distribution of NO_x emissions with a high level of detail. For future use, this method can easily be applied globally.

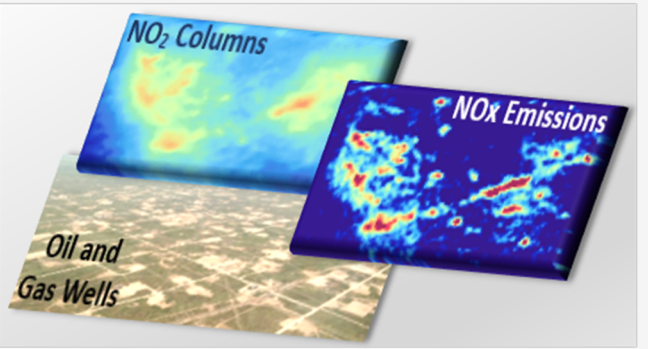

KEYWORDS: *oil and gas, emissions, nitrogen oxides, air quality, satellite, remote sensing*

1. INTRODUCTION

The widespread use of hydraulic fracturing and horizontal drilling since the mid-2000s has led to a steep rise in the production of crude oil and natural gas in the United States. Despite the economic impacts of the COVID-19 pandemic, the current national production is still near an all-time high. Associated with this activity are emissions of methane and air pollutants, such as nitrogen oxides (NO_x = NO + NO_2) and volatile organic compounds (VOCs). NO_x and VOCs are precursors for the formation of ground-level ozone, with adverse effects on human health.[1] Several oil and gas production fields in the United States are in remote areas with little or no regular air quality monitoring. In the contiguous United States, NO_x emissions from oil and gas production contribute about 5% to the total NO_x emissions,[2] but regionally, these emissions can be a significantly larger source that affects local air quality. While methane emissions from oil and gas fields have received much recent attention,[3−9] NO_x and VOC emissions are more poorly described. For example, a modeling study showed that NO_x emissions were overestimated by a factor of about 4, while VOC emissions were underestimated by a factor of about 2, in the regulatory emission inventory for the Uintah basin in Utah.[10] These discrepancies were shown to be critical in describing the occurrence of winter ozone in this basin.[11]

Bottom-up emission inventories for oil and gas operations are typically based on reported activities, which contain a high level of uncertainty. Also, being a labor-intensive product, emission inventories are often several years behind by the time of their completion. Satellites can provide easier and more up-to-date observations of emissions. Remote sensing measurements have been successfully used to infer trends in NO_x emissions over oil and gas production regions.[12−14] We use NO_2 observations from the TROPOspheric Monitoring Instrument (TROPOMI) to quantify annually averaged NO_x

Received: November 11, 2021
Revised: December 26, 2021
Accepted: January 3, 2022
Published: January 19, 2022

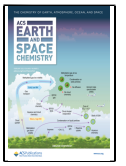

https://doi.org/10.1021/acsearthspacechem.1c00387
ACS Earth Space Chem. 2022, 6, 403−414

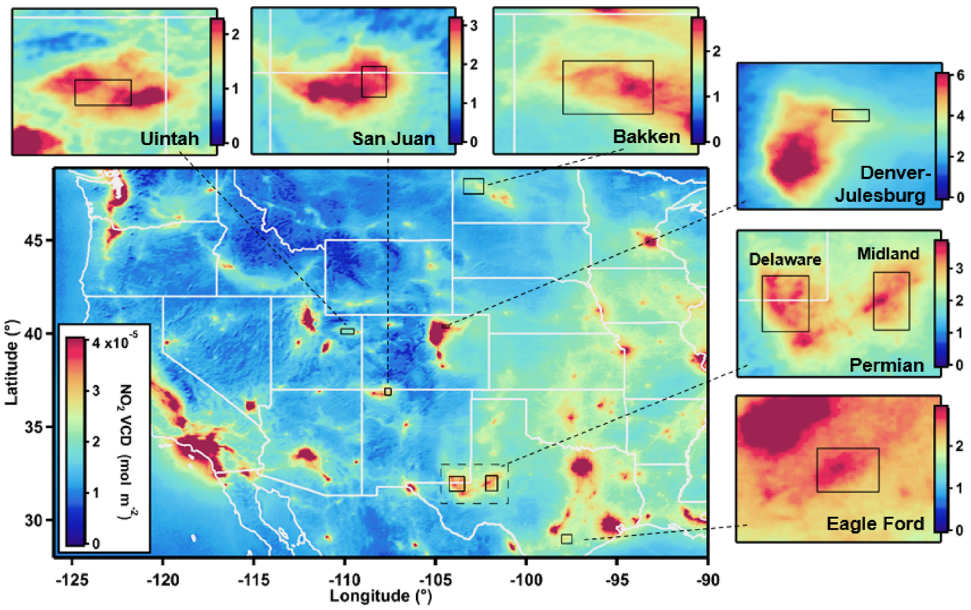

Figure 1. Tropospheric NO_2 VCDs observed by the TROPOMI satellite instrument over the continental United States averaged from 1 May 2018 to 27 December 2020. Insets provide color scale optimized maps of the oil and gas production areas analyzed here; numbers are in units of 10^{-5} mol m^{-2}. Note that the color scales differ between figure panels.

emissions from six oil and gas production regions in the United States for the years 2018, 2019, and 2020. Our method is based on recent studies by Beirle et al. that used the divergence of NO_2 column fluxes to detect and quantify NO_x emissions from point sources, such as power plants.[15,16] Here, we apply this technique to quantify NO_x area emissions from oil and gas fields. While Beirle et al. (2019) also looked at citywide emissions, to our knowledge, the NO_x divergence method has not yet been systematically evaluated by a chemistry transport model nor widely applied to calculate area emissions. We also introduce utilizing parameterized OH concentrations to calculate NO_x lifetimes, which eliminates the need for chemical model input. The advantages of this approach, referred to as the divergence method in the following, are that it is comparatively simple and computationally efficient. It is independent from atmospheric chemistry models and provides annually updated emission estimates. To evaluate our method, we compared our top-down derived emissions to NO_x emission estimates from the fuel-based inventory of oil and gas (FOG) and performed sensitivity studies on model output from the regional Weather Research Forecasting model with Chemistry (WRF-Chem). In contrast to conventional emission inventories, the FOG inventory bases its NO_x emission estimates on the volume of fuels used for drill rigs and various other engines used in pump jacks, separators, dehydrators, and compressor stations as described by Francoeur et al. (2021) and Gorchov Negron et al. (2018).[2,17] The FOG inventory was found to describe the above-mentioned NO_x emissions in the Uintah basin well and serves here as a benchmark for comparison with our satellite-derived results. To assess the accuracy of the divergence method, we ran sensitivity studies on the WRF-Chem model output and investigated the effects of individual analysis parameters such as wind fields, NO_x lifetime, or background correction. A recent study has used a similar approach to evaluate and quantify methane emissions from TROPOMI mean methane mixing ratios.[18]

Our study is structured as follows: In Section 2, we introduce data and explain our application of the divergence method. Section 3 presents the TROPOMI NO_x emission results and the comparison with the FOG inventory. In Section 4, we analyze the WRF-Chem model output and discuss error sensitivities, and final conclusions are drawn in Section 5.

2. DATA AND METHODS

The divergence method is based on the continuity equation: on a pixel-by-pixel basis, the mass flow into a given pixel plus the emissions equals the mass flow out of the pixel plus the chemical loss. The divergence of the mass flux F, ∇F, describes changes in the mass flow. A positive divergence value indicates a source. Assuming a steady state, NO_x emissions, E, can be quantified as the sum of the sources and sinks, S, as follows:

$$E = \nabla F + S = \nabla(\mathrm{sf}\cdot\mathrm{VCD}\cdot w) + \mathrm{sf}\cdot\mathrm{VCD}/\tau \quad (1)$$

Here, the mass flux, F, is two-dimensional and given by multiplication of the NO_2 vertical column density (VCD) with the horizontal wind field, w. The sink term describes a chemical loss with a constant lifetime τ. NO_2 VCDs are scaled to NO_x by a constant scaling factor, sf, of 1.32 ± 0.26, which represents a typical value for the TROPOMI overpass time and a generally polluted boundary layer.[15] Remote observations of NO_2 are frequently used as proxy for NO_x,[13,19−26] because most NO_x is emitted as NO and then rapidly converted to NO_2. In the following paragraphs, we will describe data used and our application of the method in more detail.

2.1. Data. *2.1.1. Satellite Data.* TROPOMI is a spectrometer on ESA's Copernicus Sentinel-5 Precursor satellite.[27] It has a UV−visible, a near-infrared, and a shortwave IR channel that provide simultaneous measurements of several trace gases, such as NO_2, formaldehyde, carbon monoxide, and methane. Launched in October 2017, the instrument provides daily global coverage. NO_2 is observed with a spatial resolution at nadir of 3.5 × 5.5 km^2 (3.5 × 7.0 km^2 before 6 August 2019) and analyzed in the visible wavelength range.[28] Data from 1 May 2018 onward are publicly available (http://doi.org/10.5270/S5P-9bnp8q8). Here we use version 1 of the level 2 reprocessed and offline tropospheric NO_2 VCDs from 1 May

https://doi.org/10.1021/acsearthspacechem.1c00387
ACS Earth Space Chem. 2022, 6, 403−414

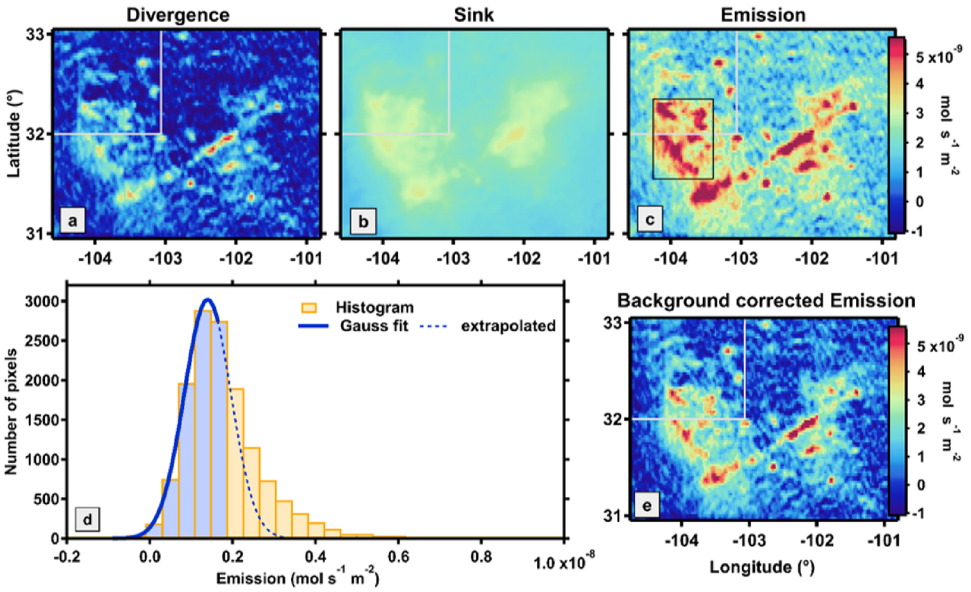

Figure 2. Calculation of NO_x emissions using TROPOMI NO_2 and the divergence method. White lines denote state lines. (a) Calculated divergence. (b) Calculated sink. (c) Calculated emissions (divergence + sink). (d) Histogram of the emissions in the Delaware basin (black box in panel c) and surrounding area and determination of the background by using a Gauss fit on the blue shaded part of the data. (e) Background corrected emissions. The data shown here are an average over the full data set from 1 May 2018 to 27 December 2020.

2018 to 27 December 2020. Tropospheric columns are derived by subtracting the stratospheric portion from the total column and are available for download as a separate operational product.[29]

NO_2 VCDs from daily orbit files are gridded on a regular latitude/longitude grid applying a surface weight. The grid has a resolution of 0.025° × 0.025°, corresponding to about 2.8 km in latitudinal direction and 2.5 km to 1.7 km in longitudinal direction between 25 and 50° latitude. Only data with a qa value (a measure for data quality) larger 0.75 are used, filtering out, among other things, cloud-covered scenes that tend to shield NO_2 close to the ground. Additionally, a solar zenith angle (SZA) filter is applied, removing data with SZA > 60°. The SZA filter minimizes tropospheric VCD errors caused by the stratospheric correction and low signal-to-noise in low light conditions.

Figure 1 shows tropospheric NO_2 VCDs averaged between 1 May 2018 and 27 December 2020. The locations of oil and gas production areas analyzed here are indicated by black boxes. For some regions, the area of interest is smaller than the production region to avoid including other NO_x sources in the analysis. For example, in the Denver-Julesburg basin, the oil and gas production region extends well into the metropolitan area, but we focus here on an area in the northeastern part of the basin where oil and gas emissions dominate over urban emissions. Likewise, power plants in the San Juan and Uintah basins dominate over oil and gas emissions and our areas of interest avoid these sources. Insets show close-ups for each study area. All selected areas show increased NO_2 columns indicative of the NO_x emissions associated with the local oil and gas production activities.

2.1.2. Meteorological Data. Meridional and zonal wind components, as well as pressure and temperature, are from the ERA-5 reanalysis from the European Centre for Medium-Range Weather Forecasts (ECMWF).[30] These data are publicly available. ERA-5 data have an hourly temporal resolution and a spatial resolution of 0.25° × 0.25° latitude/longitude. We interpolate ERA-5 data onto the NO_2 spatial grid at a constant level of 100 m above ground and interpolate in time to the local TROPOMI overpass for each study region.

2.1.3. FOG NO_x Inventory. The fuel-based inventory of oil and gas (FOG) calculates NO_x emissions for individual processes in oil and natural gas production, such as drilling, production, and processing, based on the amount of fuel used during these processes.[17] FOG data were evaluated for several oil and gas basins using aircraft measurements made during the NOAA SONGNEX study.[2] Here we use FOG inventory data for 2018 to 2020, which cover the contiguous United States and include NO_x emission estimates from natural gas flaring. For a comparison of spatial distribution maps with TROPOMI and WRF-Chem results, FOG data are gridded on the respective matching latitude/longitude grid and a two-time and one-time binomial smoothing filter is applied for TROPOMI and WRF-Chem comparisons, respectively.

2.1.4. WRF-Chem. The Weather Research and Forecasting (WRF) model coupled with Chemistry simulates emission, mixing, and chemical transformation of trace gases and aerosols simultaneously with the meteorology. Here we use the WRF-Chem output for the Permian basin (see Figure 1) from 1 June 2018 to 30 August 2018 interpolated from a 12 × 12 km^2 grid and a Lambert conformal projection onto a rectilinear latitude/longitude grid of 0.1° × 0.125° between 30 to 36° latitude and −106 to −100° longitude. The following anthropogenic emission inventories in addition to FOG are used in the WRF-Chem simulations: the Fuel-based Inventory of Vehicle Emissions (FIVE) for mobile sources,[31,32] updated power plant emissions based on stack monitoring data derived from the Continuous Emission Monitoring Systems (CEMS), and emissions for other point and areal sources from the National Emissions Inventory (NEI 2017). All WRF-Chem output data are interpolated to TROPOMI overpass times and sampled following TROPOMI NO_2 VCDs to simulate comparable cloud filtering and data coverage. WRF-Chem tropospheric NO_2 VCDs were calculated from the modeled

https://doi.org/10.1021/acsearthspacechem.1c00387
ACS Earth Space Chem. 2022, 6, 403−414

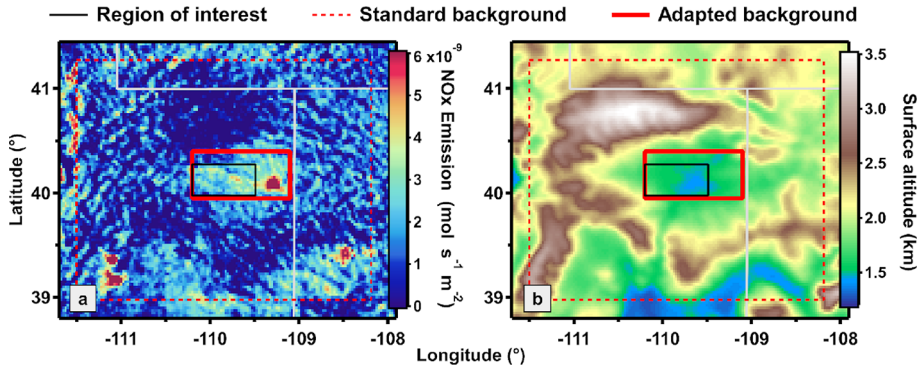

Figure 3. (a) Calculated NO_x emissions for the year 2020 and (b) surface altitude for the Uintah basin. White lines denote state lines. The adapted background borders (solid red lines) follow emissions deemed representative for the valley NO_2 background and keep surface altitude changes to within 550 m. NO_x emissions outside the updated background border quickly fall off and even drop below zero, which would create a high bias in the calculated NO_x emissions if the standard background area (red dashed lines) was used.

NO_2 vertical profiles, summing partial VCDs from the surface to the tropopause temperature minimum. Boundary layer VCDs were cut off at the boundary layer height provided by the WRF-Chem output. Displayed WRF-Chem other anthropogenic NO_x emissions are weekday emissions from July 2018 averaged over 3 h around the TROPOMI overpass time.

2.2. Methods. *2.2.1. Divergence.* The divergence term in eq 1 is calculated as the derivative of the zonal and meridional scaled NO_2 column fluxes. The derivative is approximated as a second-order central difference. The divergence is calculated for daily NO_x fluxes and averaged annually. We assume that the free tropospheric NO_2 fraction above the planetary boundary layer, PBL, is sufficiently constant over each study area to not significantly affect the divergence. The absolute magnitude of the column above the PBL is irrelevant, because the derivative of a constant is zero. Accordingly, we treat the divergence as indicative of emissions in the PBL.

Figure 2a shows an example of a divergence map, calculated for the Permian basin (see Figure 1), which contains the largest oil and natural gas production in the United States. Positive divergence values indicate net source areas. Negative values mostly arise from the chemical loss, which will be accounted for by the sink term, but can also be artifacts caused by errors in the wind fields, statistical noise, or violation of the steady state.

2.2.2. Sink. The overpass time of the TROPOMI satellite instrument around 13:30 local time allows the assumption that the chemical loss of NO_x is dominated by the reaction with the hydroxyl radical, OH.[15] We approximate an effective lifetime, τ, as first-order loss to OH:

$$\tau = 1/(k_{OH+NO2}\cdot[OH]) \quad (2)$$

The rate constant k_{OH+NO2} is calculated following the Master Chemical Mechanism,[33,34] MCM, using pressure and temperature from ECMWF. The sink term is then calculated according to eqs 1 and 2. Even though the instantaneous NO_x lifetime is a complex function of NO_x and VOC concentrations as well as temperature, pressure, and photolysis frequencies, constant NO_x lifetimes have been found to be a suitable concept to relate remotely observed NO_2 VCDs to NO_x emissions.[20,22,25]

To keep our approach simple and independent from atmospheric chemistry models, OH concentrations are calculated based on the empirical relationship between the photolysis frequency of ozone and OH as observed and described by Rohrer and Berresheim.[35] Ozone photolysis with a frequency $J(O(^1D))$ produces excited $O(^1D)$ atoms, which form OH in reaction with water. The authors empirically derived a mostly linear correlation between $J(O(^1D))$ and OH that holds true across different seasons and locations, although slopes and offsets of the applied line fits vary. For our study, we use line fit parameters averaged across all described campaigns:

$$[OH] = 3.38\cdot10^6\cdot(J(O(^1D))\cdot10^5)^{0.956} + 0.162\cdot10^6 \quad (3)$$

where $[OH]$ is in units of 10^6 cm^{-3} and $J(O(^1D))$ is in 10^{-5} s^{-1}. $J(O(^1D))$ itself is a function of SZA and calculated following the MCM.[34,36] Here, the SZA cutoff at 60° applied to the NO_2 VCDs is important to exclude the very long NO_2 lifetimes at high SZAs. The calculated sink term for the Permian basin is shown in Figure 2b, and the resulting NO_x emissions for the same area (divergence plus sink) are displayed in Figure 2c. Negative values in the divergence map (Figure 2a) caused by chemical loss are mostly accounted for by the addition of the sink term. The sink term is calculated from the tropospheric NO_2 VCDs and therefore contains a boundary layer and free tropospheric NO_2 background, which needs to be subtracted to get net emissions from the oil and gas production activities. We quantify this background based on the NO_x emissions maps as explained in the following.

2.2.3. Background Correction. For each region of interest (black boxes in Figure 1), we take the surrounding area as a measure for the NO_2 background contained in the VCDs. Based on sensitivity studies, we extend the region of interest by 111 km in each direction (1° latitude and corresponding longitude) and create a histogram from the NO_x emission data as shown in Figure 2d. A constant regional background appears as a normal distribution with local emissions on top of the regional background, creating a tail toward higher values, as seen in Figure 2d. We apply a Gauss fit to the left side of the histogram by constraining the fit on the right side to the *y*-maximum plus one more point, as indicated by the blue shaded area in Figure 2d. The fitted peak value quantifies the regional background. Details on histogram settings are provided in Section S1. The background corrected NO_x emissions map is presented in Figure 2e. As expected, emissions of the surrounding area are now around zero.

While the divergence is calculated daily, background correction values for the annual NO_x emission averages presented in Section 3 are derived from their corresponding annually averaged emission maps. Annual data inherently

https://doi.org/10.1021/acsearthspacechem.1c00387
ACS Earth Space Chem. 2022, 6, 403−414

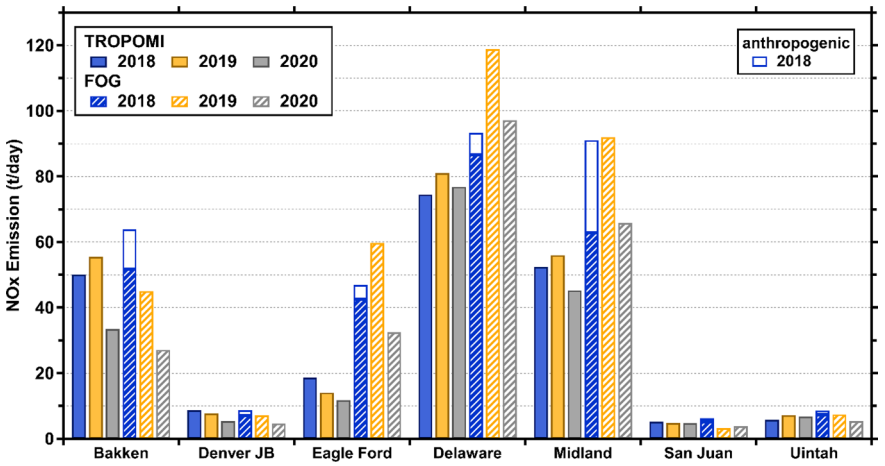

Figure 4. NO_x emissions for the years 2018 to 2020, calculated from TROPOMI data (solid bars) and from the FOG inventory (striped bars), and other anthropogenic NO_x emissions for 2018 (open bars).

average over the seasonal cycle in NO_x. The 2018 NO_2 data, however, only start in May, which affect the magnitude of the sink term and background correction. To assess and account for this effect, we calculated NO_x emissions for 2019 from May to December for each study area and used the difference to the 2019 12-month average as a correction factor for the 2018 data. Correction factors range between −23 and +28%.

Local topography and surrounding NO_2 conditions can complicate the background corrections. For example, the San Juan and Uintah production regions are both located in mountain valleys, where boundary layer air can get trapped. Slopes at the valley sides create complex meteorological patterns that are not well resolved by the 0.25° resolution of the ECMWF wind fields, and strong altitude gradients add to the uncertainty of the TROPOMI NO_2 VCD retrievals. These factors increase the uncertainty in the divergence and sink terms. Further, NO_2 VCDs over the surrounding mountains do not contain the background NO_2 inside the valley, which create a low bias in the subtracted background and lead to a high bias in the calculated NO_x emissions. Figure 3a shows NO_x emissions that are not yet background corrected, calculated for the Uintah basin for 2020 next to the surface elevation in panel b. Red dashed lines indicate the standard background area, while the red solid line shows what we call an adapted background region, which includes only emissions that are on average larger than 2×10^{-9} mol s^{-1} m^{-2}, and surface altitude changes inside the adapted background region are within 550 m of the region of interest (black box in Figure 3). NO_x emissions outside the updated background border quickly fall off and even drop below zero. Emissions for the Uintah, San Juan, and Delaware basins were all calculated with an updated background (see Figures S1 and S2 for the San Juan and Delaware adapted backgrounds).

2.2.4. Quantification of NO_x Emissions. The net NO_x emissions for each study area are quantified as the sum of background corrected emissions above zero within the region of interest. The borders of each study area were optimized to include significant signals over production areas and exclude other significant NO_x sources, but some contamination from other sources might remain. As part of our analysis for the Permian basin, we also quantified selected point sources. This was done by fitting a two-dimensional Gaussian to the point source area within a radius of 12 km and calculating emissions as the volume of the fitted Gaussian.

3. RESULTS

3.1. TROPOMI Results and Comparison with the FOG NO_x Inventory. Applying the methods described above, we calculated annually averaged NO_x emissions for 2018, 2019, and 2020 for six oil and natural gas production areas in the United States (see Figure 1). Results are displayed in Figure 4 as solid bars (see Figure S3 for uncorrected TROPOMI 2018 data).

Emissions calculated from the TROPOMI analysis over all 3 years range between 4.8 and 81.1 t/day. The Bakken, Delaware, Midland, and Uintah basins show increasing emissions from 2018 to 2019 followed by a decrease from 2019 to 2020. These trends are consistent with the continued growth of U.S. oil and natural gas production up until the start of the lockdowns in March 2020 due to the COVID-19 pandemic.[37,38] While the consumption of natural gas was less affected in 2020, the demand for oil dropped rapidly, leading to a particularly stark decline in the drilling of new wells and reduced production.[39] With a drop of 40%, the Bakken basin, which is predominantly an oil-producing region, shows the strongest observed decline in 2020. Denver-Julesburg, Eagle Ford, and San Juan show declining NO_x emissions from 2019 to 2020 as well, but here, and in the Uintah basin, the observed differences are small and might also be affected by the general decline of anthropogenic NO_x in 2020 due the COVID-19 pandemic. In contrast, the Permian (Delaware and Midland) and Bakken basins are located in more remote areas and have comparatively high NO_x emissions. Here, it is safe to assume that observed trends are more directly correlated with changes in the local oil and gas production activities. The TROPOMI tropospheric NO_2 VCDs used here tend to have a low bias over polluted regions, which is on the order of 20% for areas comparable to our study areas[40] and possibly more when used with the divergence method to retrieve NO_x emissions close to the ground.[15,16] Our calculated NO_x emissions are therefore likely a lower limit.

FOG NO_x emissions for the same years and locations are included in Figure 4, as well as other anthropogenic NO_x emissions for 2018 (see Section 2.1). TROPOMI and FOG NO_x emissions track each other well across study areas and over time. Emissions agree on average within 12 ± 24% (2018), 11 ± 41% (2019), and 4 ± 35% (2020). The agreement in 2018/2019/2020 is better for the Bakken (3/23/

https://doi.org/10.1021/acsearthspacechem.1c00387
ACS Earth Space Chem. 2022, 6, 403−414

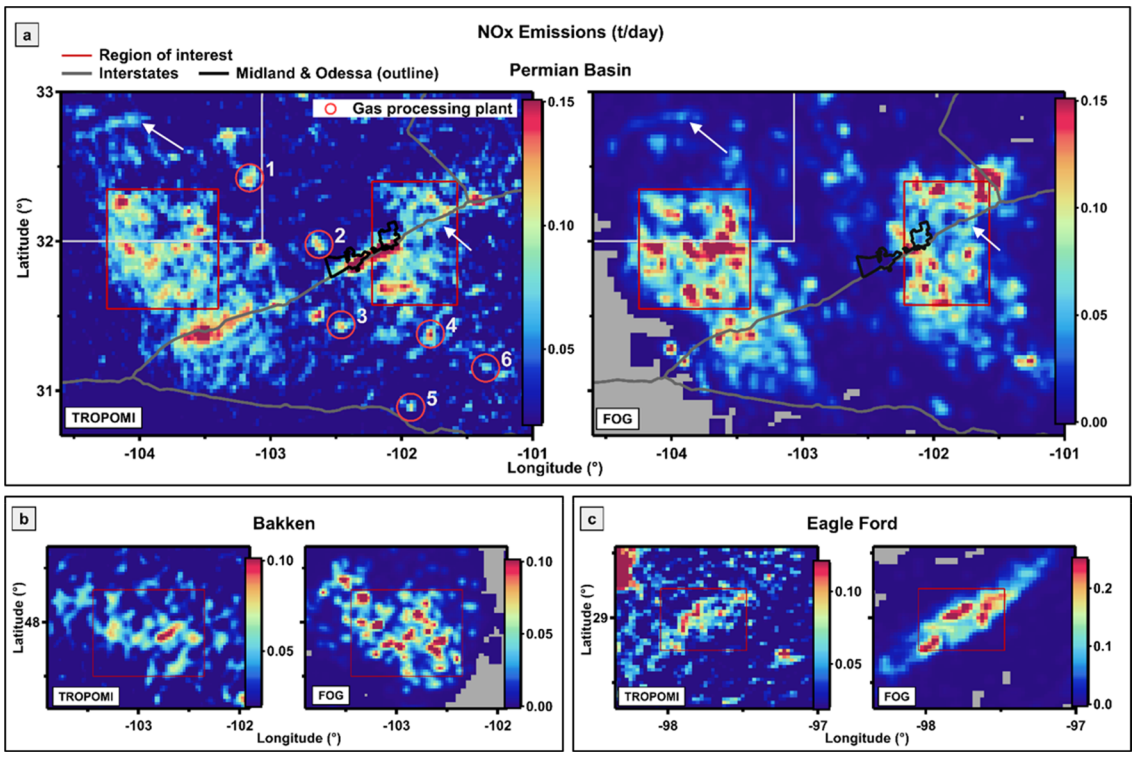

Figure 5. NO_x emissions calculated from 2018 TROPOMI NO_2 VCDs next to FOG emissions (i.e., oil and gas emissions only) for the (a) Permian (Midland and Delaware) basin, (b) Bakken basin, and (c) Eagle Ford basin. White lines denote state lines. TROPOMI results for the Bakken basin have a one-time binomial smoothing applied. Regions of interest are labeled with red boxes. The TROPOMI Permian basin map is created with the Delaware background correction, and red circles with white numbers indicate gas processing plants for which NO_x emissions have been calculated (see Section 3.2). White arrows point out unique spatial features in the Permian basin that exist in both TROPOMI-calculated and FOG NO_x emissions.

23%) and Delaware (14/32/21%) basins than for the Midland (17/40/31%) and San Juan (45% in 2019) regions, likely because other NO_x sources are relatively more important (Midland) or because of the mountain topography (San Juan). Eagle Ford shows the strongest deviation from FOG, being smaller by 56/76/64%. The Eagle Ford basin is located close to San Antonio and is surrounded by a comparatively high NO_2 background (see Figure 1). At the same time, FOG NO_x emissions here have the highest emission per area average compared to other study areas. It is possible that a fraction of such high-density emissions is diluted into the background before it has a chance to appear on top of the background as structured emissions plumes, which get quantified by the divergence. As a result, this fraction would be mostly canceled out during the background correction.

In 2018, the fraction of anthropogenic NO_x emissions compared to FOG is below 24% for all basins except for the Midland basin (37%), which supports that NO_x emissions from oil and gas production are the dominant NO_x source in our selected study areas. These other emissions from transportation and industrial activity are not expected to significantly change in 2019 or 2020.

To illustrate the spatial information contained in the calculated emission maps, Figure 5 shows NO_x emissions calculated from TROPOMI 2018 NO_2 VCDs next to FOG NO_x emissions for the Permian (Midland and Delaware), Bakken, and Eagle Ford basins. Note that TROPOMI calculated emission maps include the detection of other NO_x sources as well, while FOG emission maps only show the oil and gas production related NO_x emissions. For all three basins, we find agreements between TROPOMI and FOG in co-location of gradients and emission hot spots within the regions of interest. The Permian basin (Figure 5a) shows a particularly high level of spatial detail and excellent agreement with FOG NO_x emissions. Exemplary features are pointed out by white arrows in both maps: an "arc" of NO_x emissions to the northwest of the Delaware basin and a ring-shaped emission pattern in the north of the Midland basin (the interstate, gray line, is going through the lower half of the ring). The largest cities in the Permian basin are Midland and Odessa (black outlines in Figure 5a). Midland is located within the Midland region of interest, but has small NO_x emissions within city limits compared to Odessa, which was excluded from the region of interest. As the TROPOMI map shows, most urban NO_x emissions are located along the interstate. The Midland region of interest boundaries are a compromise between including areas with high oil and gas production (see FOG map), while still excluding significant urban signals. Compared to the Delaware basin though, calculated Midland NO_x emissions contain a higher fraction of urban NO_x emissions, which could explain the stronger NO_x emission fall off seen in 2020 (Figure 4). The TROPOMI-derived NO_x emission map also indicates the presence of point sources in the Permian basin, some of which are gas processing plants. Red circles mark gas plants for which we quantified NO_x emissions from the TROPOMI NO_2 observations. Results are presented and discussed in Section 3.2. NO_x emissions calculated for the Bakken basin (Figure 5b) agree well with FOG in tracing the contours of the highest production emissions and show co-located hotspots despite having poorer data statistics compared

https://doi.org/10.1021/acsearthspacechem.1c00387
ACS Earth Space Chem. 2022, 6, 403−414

to other basins. Being farthest north, NO_2 VCDs over the Bakken basin are most impacted by SZA and snow/ice filtering. The comparison for the Eagle Ford basin (Figure 5c) shows some discrepancies in the location of hot spots, and calculated emissions are overall lower than FOG. However, sharp gradients in the emission maps are detected and quantified by the divergence term, whereas features in the sink term are diluted by atmospheric transport. While the sink term is important for the accuracy of the total NO_x emission estimates, it is safe to assume that gradients on sub-basin scales can be detected with a precision that exceeds the accuracy of the absolute NO_x quantification.

Generally, differences between TROPOMI and FOG can be caused by several reasons: Cloud and SZA filtering leads to uneven data statistics in TROPOMI NO_2 VCDs, leaving some areas within a region of interest possibly undersampled. Another reason could be that drill rigs are not stationary NO_x sources, because the drilling of a new well takes on the order of weeks to months, after which the drill rig moves to another site. Uneven sampling of the NO_2 VCDs could miss some of the drilling activity. With respect to the FOG inventory, possible reasons for discrepancies could be that emissions are assumed to be consistent across a 24-h daily cycle, which might not be the case. Further, state-level fuel volumes are distributed across wells by production as a proxy. Especially for a large state like Texas with multiple oil and gas production basins, this could be an important source of spatial uncertainty. Despite these potential uncertainties, the TROPOMI-derived emission maps provide valuable information on the spatial distribution of NO_x emissions from oil and gas production activities, especially for areas with higher emissions, such as the Permian basin.

3.2. NO_x Emissions from Gas Processing Plants. Gas processing plants are an integral part of the infrastructure in areas with natural gas production. In the Permian basin, NO_x emissions of some gas plants are sufficiently large to appear as a point source in the TROPOMI NO_x emission map (red circles in Figure 5a). We quantified NO_x emissions for those gas plants that have no other known significant NO_x sources close by. Calculated annual emissions for 2018 to 2020 are given in Table 1 together with emissions from the National Emissions Inventory 2017 (NEI 2017).

Table 1. NO_x Emissions of Gas Processing Plants Reported in t/day

number in Figure 5a	NEI 2017	TROPOMI 2018	TROPOMI 2019	TROPOMI 2020
1	3.3	3.3	2.3	1.6
2	2.0[a]	2.1	1.6	1.6
3	3.2	1.5		0.9
4	0.7[b]	1.6	1.6	2.2
5	1.8	0.7	1.0	1.3
6	0.2	0.8	1.3	1.2

[a]Two plants side by side: (1.85 + 0.15) t/day. [b]Two plants side by side: (0.6 + 0.1) t/day.

NO_x emissions calculated from TROPOMI observations for the selected gas processing plants are in the same order of magnitude as NEI stated emissions and agree on average within 1 t/day. Given the reported low bias of TROPOMI NO_2 columns (see above), the calculated NO_x emissions for the gas processing plants are likely a lower limit. The total NO_x emissions for these six gas processing plants are 9.9, 7.6, and 8.7 t/day for the years 2018, 2019, and 2020. Figure S4 shows all NEI 2017 gas processing plant emissions together with the FOG emissions for the Permian basin. Based on the NEI 2017, total NO_x emissions from all gas processing plants shown in Figure S4 are 36.9 t/day, with 0.8 t/day inside the Delaware region of interest and 5.1 t/day inside the Midland region of interest. These results indicate that gas processing plants are a significant source of NO_x emissions in the Permian basin.

4. EVALUATION OF THE DIVERGENCE METHOD USING THE WRF-CHEM OUTPUT

The WRF-Chem model output provides the opportunity to evaluate the accuracy of total area NO_x emissions calculated with the divergence method since the model input emissions are known. It also allows one to individually study the effect of analysis parameters on retrieved NO_x. Figure 6 shows an example of NO_x emissions calculated for the Delaware basin using the divergence method on WRF-Chem modeled NO_2 VCDs. Derived emissions are shown in the left panel next to FOG emissions (middle panel) and FOG together with all other NO_x sources (right panel) that were included in the WRF-Chem run as input. The WRF grid does not allow one to resolve a lot of details on sub-basin scales, but the main features are still reproduced with the divergence method. The WRF-Chem modeled NO_2 VCDs change more strongly across the Permian basin in east−west direction compared to what is observed in the annual TROPOMI VCDs, which explains the seemingly overestimated NO_x emissions in the Midland basin in Figure 6 when shown with the Delaware background correction. Because of this stronger gradient, the background region for the Delaware basin was readjusted (see Figure S5). The comparatively coarse resolution of the WRF-Chem model also leads to poor histogram data statistics. To account for the resulting larger uncertainties, the background correction value was determined by taking the median value over several histogram fits with slightly different settings. For further details, see Section S2.

Calculated NO_x emissions for the Delaware (Figure 6) and Midland (Figure S6) basins agree with the FOG input emission to within 2 and 8%, respectively. Uncertainties created by moving the region of interest borders within plus and minus one of the now larger pixels are on the order of 5%. The map of FOG and other NO_x sources in Figure 6 illustrates the dominance of oil and gas production NO_x sources, especially in the Delaware basin, where FOG emissions account for 83% of the total NO_x emissions. The NO_x emissions displayed in Figure 6 and Figure S6 were calculated using WRF-Chem wind fields at 100 m above ground. The NO_x lifetime was calculated following eq 2, using WRF-Chem OH, pressure, and temperature at wind level altitude. WRF-Chem NO and NO_2 concentrations at wind level altitude determined the NO_x scaling factors. We call this setup the base case. To study the effect of individual parameters on divergence method results, single parameters were systematically changed from the base case as outlined in Table 2.

4.1. Results of the WRF-Chem Sensitivity Studies. The results of the sensitivity studies are summarized in Figure 7. Calculated NO_x emissions for the Delaware and Midland basins are presented as percent changes to the FOG input emissions. Results across all sensitivity studies remain within 20% of the input emissions, which are highly encouraging with respect to using the divergence method for the quantification

https://doi.org/10.1021/acsearthspacechem.1c00387
ACS Earth Space Chem. 2022, 6, 403−414

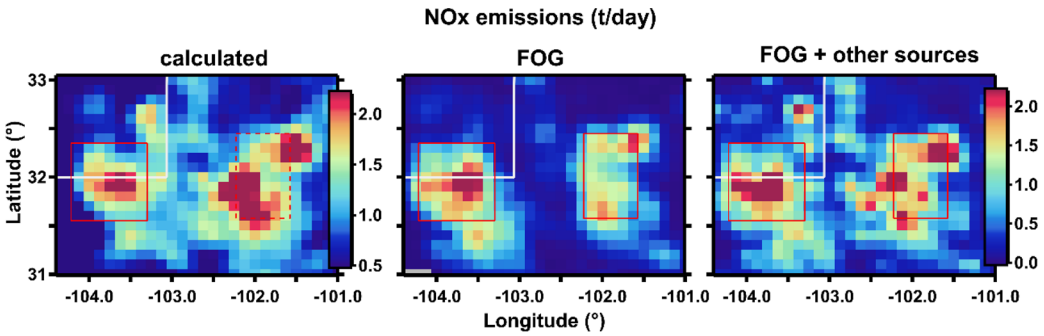

Figure 6. NO_x emissions calculated with the divergence method for the Delaware basin from the WRF-Chem output next to the model input NO_x emissions. White lines denote state lines. Red boxes mark regions of interest. NO_x emissions shown here are calculated with the background correction of the Delaware basin, which creates the appearance of a high bias for the Midland basin in this figure (red dashed line).

Table 2. WRF-Chem Sensitivity Studies

case study	background correction	wind level	wind source	NO_x lifetime	NO_x scaling	NO_2 VCD
base	median	100 m	WRF	[OH]	$[NO_x]/[NO_2]$	tropospheric
			Changes to base case			
1) bg. corr.	± sdev					
2) 400 m		400 m				
3) PBL avg.		PBL avg.				
4) ECMWF			ECMWF			
5) OH param.				param. OH		
6) sf = 1.32					1.32	
7) VCD PBL						PBL
8) TROPOMI			ECMWF	param. OH	1.32	

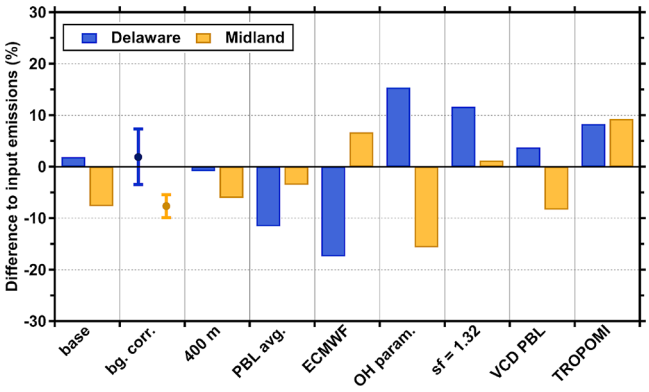

Figure 7. Results of the WRF-Chem sensitivity studies for the Delaware and Midland basins for all cases stated in Table 2 and expressed as percent difference to FOG input emissions.

of area sources. The strongest deviations from the input emissions are seen for changes in the wind fields and in the NO_x lifetime. In the following, we will explain these results in more detail and discuss them in the context of our TROPOMI analysis.

1) Background correction: The standard deviation across the set of histogram fits that determine the background value (see Section S2) is used to calculate the random error caused by the background correction. Shown in Figure 7, in the "bg. corr" column, are the uncertainties for the base case, which are 5.4 and 2.2% for the Delaware and Midland basin, respectively. Background uncertainties for all WRF-Chem cases expressed as differences to the originally calculated NO_x emissions are on average 11 ± 5% (Delaware) and 4 ± 1% (Midland).

2,3) Wind level: Changes in calculated NO_x emissions from using different wind levels ("400 m" and "PBL avg.") are <13%. The small spread in results indicates that using wind speeds at fixed levels is a suitable approximation of the model boundary layer wind fields and that the actual choice of altitude does not lead to significant changes. These findings are consistent with previous studies.[15,16] The boundary layer height used to create the PBL averaged wind fields is from WRF-Chem itself and therefore consistent with the modeled NO_2 VCDs. When using modeled PBL heights in combination with satellite data, resulting errors could be larger when real and modeled PBL heights do not match.

4) Wind source: Using ECMWF wind fields tests the effects of deviations from the model wind. Over the Midland basin and most of its background area, ECMWF wind speeds are generally higher than WRF wind speeds, i.e., the actual wind in the model, but are mostly consistent in direction. Resulting NO_x emissions are higher compared to the base case. Over the Delaware basin, conditions are more complex and the ECMWF and WRF wind fields differ in speed and direction. The calculated NO_x emission map for this case, see Figure S7, shows that NO_x emissions from the Delaware basin appear to be shifted and partially moved out of the region of interest, which create a low bias and poor co-location with the FOG input emissions.

5) NO_x lifetime: Here we investigate the effect of using either OH parameterized by the solar zenith angle or WRF-Chem modeled OH concentrations that include the effects of atmospheric chemistry and show a dependency on NO_x concentrations and surface altitude. We assume here that the difference is also representative

https://doi.org/10.1021/acsearthspacechem.1c00387
ACS Earth Space Chem. 2022, 6, 403−414

for the difference between parameterized and actual OH in the atmosphere. NO_x lifetimes based on WRF-Chem OH concentrations are on average 5.1 and 3.0 h for the Delaware and Midland basin, respectively, with lifetimes increasing from 3 to 7 h across the Delaware background region. Lifetimes based on parameterized OH concentrations are 3.7 and 2.9 h, respectively, with negligible dependence on surface altitude (see Figure S8 for lifetimes). Changes in the NO_x lifetime only affect the sink term, where a shorter lifetime leads to a larger sink term. The effects on the calculated total NO_x emissions seen in Figure 7 are determined by the relative changes in lifetime between the region of interest and the background areas. For the Delaware basin, the increase of the sink term leads to an increase in total NO_x emissions, while for the Midland basin, a net decrease in calculated NO_x emissions is created by the now relatively larger background. Despite the large lifetime differences, retrieved NO_x emissions are within 16% of FOG input emissions, which indicate that our background correction does compensate even for larger differences and that using parameterized OH concentrations is a suitable method for our application.

6) NO_x scaling factor: The scaling factor based on the WRF-Chem simulated NO and NO_2 concentrations is on average 1.22 for both the Delaware and Midland basins for the base case and thus within the given range of ±0.26 for the constant NO_x scaling factor of 1.32 used in the TROPOMI analysis (see Section 2). The difference of 8% in the scaling factor translates to a difference in calculated NO_x emissions of the same magnitude. We assume that this difference is also representative of the difference between the factor of 1.32 used in the divergence method vs the actual NO_x–NO_2 ratio in the atmosphere.
7) Tropospheric vs PBL VCDs: The divergence method uses tropospheric VCDs as a representation of NO_2 in the boundary layer, mainly because VCDs containing only boundary layer NO_2 are not a product that is easily available. Calculated NO_x emissions using WRF-Chem PBL VCDs are less than 2% different from the base case, indicating that the free tropospheric fraction contained in the tropospheric NO_2 VCDs is approximately constant and canceled out by the background correction. This premise might not hold true for TROPOMI NO_2 VCDs across the board, but the magnitude of the background uncertainty (see above) is a good indicator for the stability of the NO_2 background across the region of interest and background area.
8) TROPOMI settings: Here we tested the effect of applying all parameters used for TROPOMI analysis simultaneously, i.e., ECMWF wind fields, parameterized OH, and a NO_x scaling factor of 1.32. Deviations in resulting NO_x emissions from the base case are smaller than some of the individual deviations, e.g., case ″ECMWF″ or ″OH param.″, which indicate that individual errors with a different sign can compensate each other.

4.2. Discussion of Sensitivity Study Results in the Context of TROPOMI Data. Our sensitivity studies show that the choice of wind level altitude and the NO_x to NO_2 scaling factor are smaller potential error sources, which are consistent with prior studies.[15,16] The background correction, choice of wind fields, and OH lifetime can create larger errors in the calculated NO_x emissions. The calculated uncertainty of the background correction is a good indicator to assess the magnitude of the error created by the background correction. Background uncertainties in TROPOMI data expressed as differences to the originally calculated NO_x emissions are 15 ± 9%, averaged over all study areas and years, or 3 ± 2 t/day, which is a bit larger than what the WRF-Chem sensitivity study shows. Smaller study areas are more sensitive to the background uncertainty as well as study areas with strongly changing topography. For the latter, this effect can be mitigated by adapting the background region. Errors in the wind fields can create artifacts in the divergence map[15,16] or lead to poor spatial correlation between the calculated and input emissions locations, such as for the Delaware basin ″ECMWF″ case. Both indicators can be used for data quality filtering. The application of the divergence method to calculate NO_x emissions assumes a steady state, which means no changes in the wind direction and constant NO_x emission across the region of interest. Even though the divergence is calculated daily, this assumption does not hold true everywhere. Areas with known systematic diurnal cycles of wind direction are not well suited for application of the divergence method. Likewise, areas with a complex mesoscale meteorology that is not resolved by the spatial resolution of the wind fields are not good candidates for the divergence method either. Annual NO_x lifetimes calculated for the TROPOMI regions of interest range between 3.9 and 4.6 h, which are consistent with other studies that use effective NO_x lifetimes to relate NO_2 VCDs to NO_x emissions.[20,22,25] The WRF-Chem sensitivity study for the Delaware basin showed that results using the parameterized OH are within 13% of using WRF-Chem OH, even though the latter has a much larger variability across the region of interest and background area. Uncertainties in the lifetime affect only the sink term. Therefore, the error on the calculated NO_x emissions is mitigated by the fraction that the sink term contributed to the total emissions. All significant error sources identified here are systematic and would not be reduced by increased time averaging.

5. CONCLUSIONS

We calculated annually averaged total NO_x emissions for six oil and gas production areas in the United States. The comparison of our results to the FOG NO_x inventory showed good agreement in magnitude and trends over time. NO_x emissions agreed within 12 ± 24% (2018), 11 ± 41% (2019), and 4 ± 35% (2020). The general consistency between TROPOMI-calculated NO_x emissions and FOG speaks to the fact that NO_x emission retrievals using the divergence method on TROPOMI NO_2 tropospheric VCDs are successful across a range of different meteorological and atmospheric conditions (between latitude 28 and 49°) and across challenging topography. The observed consistency of local gradients between FOG and TROPOMI demonstrates the value of the spatial information contained in the calculated emission maps and confirms that enhancements in NO_2 VCDs indeed correlate with the intensity of industrial activity, as have been shown in prior studies.[12−14] The evaluation of our method with WRF-Chem model results led us to conclude that the divergence method is a useful tool for the retrieval of total NO_x emissions from oil and gas production activities for a

https://doi.org/10.1021/acsearthspacechem.1c00387
ACS Earth Space Chem. 2022, 6, 403−414

range of different analysis parameter settings. Based on the combined analysis from Sections 3 and 4, we conclude that total NO_x emissions from oil and gas production areas can be calculated on an annual basis for most cases within an uncertainty of 50%. Further, calculated NO_x emission maps can provide a high level of spatial detail with a precision that likely exceeds the accuracy of the total NO_x quantification. Given the large uncertainties and time lag in general bottom-up emission inventories for oil and gas operations, the divergence method is an excellent tool to 1) provide timely emissions data, e.g., for the use in chemistry transport models; 2) evaluate bottom-up emission inventories; 3) follow trends in time, such as the effects caused by the COVID-19 lockdowns; and 4) provide information on the spatial distribution of NO_x emissions with a high level of detail. For future use, this analysis can easily be expanded globally to quantify NO_x emissions from oil and gas production activities in areas where no other emission information is available. Next steps will include building and expanding upon prior work[2,41] that uses observed NO_2 to methane ratios to scale from NO_x to methane emissions.

■ ASSOCIATED CONTENT

Supporting Information

The Supporting Information is available free of charge at https://pubs.acs.org/doi/10.1021/acsearthspacechem.1c00387.

Information on background correction; uncorrected TROPOMI NO_x emissions for 2018; NEI 2017 gas processing plants emissions; WRF-Chem sensitivity study results for base case Midland basin and case 4); NO_x lifetime comparison (Sections S1 and S2, Figures S1−S8) (PDF)

■ AUTHOR INFORMATION

Corresponding Author

Barbara Dix − *Cooperative Institute for Research in Environmental Sciences, University of Colorado, Boulder, Colorado 80309, United States;* orcid.org/0000-0001-6753-8620; Email: barbara.dix@colorado.edu

Authors

Colby Francoeur − *Cooperative Institute for Research in Environmental Sciences and Department of Mechanical Engineering, University of Colorado, Boulder, Colorado 80309, United States; NOAA Chemical Sciences Laboratory, Boulder, Colorado 80305, United States;* orcid.org/0000-0003-4491-7462

Meng Li − *Cooperative Institute for Research in Environmental Sciences, University of Colorado, Boulder, Colorado 80309, United States; NOAA Chemical Sciences Laboratory, Boulder, Colorado 80305, United States*

Raquel Serrano-Calvo − *Department of Civil Engineering and Geosciences, Technical University of Delft, 2628 CN Delft, The Netherlands*

Pieternel F. Levelt − *Department of Civil Engineering and Geosciences, Technical University of Delft, 2628 CN Delft, The Netherlands; NCAR Atmospheric Chemistry Observations & Modeling Laboratory, Boulder, Colorado 80307, United States; Royal Netherlands Meteorological Institute, 3731 GA De Bilt, The Netherlands*

J. Pepijn Veefkind − *Department of Civil Engineering and Geosciences, Technical University of Delft, 2628 CN Delft, The Netherlands; Royal Netherlands Meteorological Institute, 3731 GA De Bilt, The Netherlands*

Brian C. McDonald − *NOAA Chemical Sciences Laboratory, Boulder, Colorado 80305, United States;* orcid.org/0000-0001-8600-5096

Joost de Gouw − *Cooperative Institute for Research in Environmental Sciences and Department of Chemistry, University of Colorado, Boulder, Colorado 80309, United States;* orcid.org/0000-0002-0385-1826

Complete contact information is available at: https://pubs.acs.org/10.1021/acsearthspacechem.1c00387

Notes

The authors declare no competing financial interest.

■ ACKNOWLEDGMENTS

This work was financially supported by the NASA ACMAP program under award number 80NSSC19K0979. We acknowledge funding from the Rocky Mountain Institute and Blue Sky Resources.

■ REFERENCES

(1) Jerrett, M.; Burnett, R. T.; Pope, C. A.; Ito, K.; Thurston, G.; Krewski, D.; Shi, Y.; Calle, E.; Thun, M. Long-Term Ozone Exposure and Mortality. *N. Engl. J. Med.* **2009**, *360*, 1085−1095.

(2) Francoeur, C.; McDonald, B. C.; Gilman, J. B.; Zarzana, K. J.; Dix, B.; Brown, S. S.; de Gouw, J. A.; Frost, G. J.; Li, M.; McKeen, S. A.; Peischl, J.; Pollack, I. B.; Ryerson, T. B.; Thompson, C.; Warneke, C.; Trainer, M. Quantifying Methane and Ozone Precursor Emissions from Oil and Gas Production Regions across the Continental US. *Environ. Sci. Technol.* **2021**, *55*, 9129−9139.

(3) Alvarez, R. A.; Zavala-Araiza, D.; Lyon, D. R.; Allen, D. T.; Barkley, Z. R.; Brandt, A. R.; Davis, K. J.; Herndon, S. C.; Jacob, D. J.; Karion, A.; Kort, E. A.; Lamb, B. K.; Lauvaux, T.; Maasakkers, J. D.; Marchese, A. J.; Omara, M.; Pacala, S. W.; Peischl, J.; Robinson, A. L.; Shepson, P. B.; Sweeney, C.; Townsend-Small, A.; Wofsy, S. C.; Hamburg, S. P. Assessment of Methane Emissions from the U. S. Oil and Gas Supply Chain. *Science* **2018**, *361*, 186−188.

(4) Duren, R. M.; Thorpe, A. K.; Foster, K. T.; Rafiq, T.; Hopkins, F. M.; Yadav, V.; Bue, B. D.; Thompson, D. R.; Conley, S.; Colombi, N. K.; Frankenberg, C.; McCubbin, I. B.; Eastwood, M. L.; Falk, M.; Herner, J. D.; Croes, B. E.; Green, R. O.; Miller, C. E. California's Methane Super-Emitters. *Nature* **2019**, *575*, 180−185.

(5) Tullos, E. E.; Stokes, S. N.; Cardoso-Saldana, F. J.; Herndon, S. C.; Smith, B. J.; Allen, D. T. Use of Short Duration Measurements to Estimate Methane Emissions at Oil and Gas Production Sites. *Environ. Sci. Technol. Lett.* **2021**, *8*, 463−467.

(6) Lyon, D. R.; Hmiel, B.; Gautam, R.; Omara, M.; Roberts, K. A.; Barkley, Z. R.; Davis, K. J.; Miles, N. L.; Monteiro, V. C.; Richardson, S. J.; Conley, S.; Smith, M. L.; Jacob, D. J.; Shen, L.; Varon, D. J.; Deng, A.; Rudelis, X.; Sharma, N.; Story, K. T.; Brandt, A. R.; Kang, M.; Kort, E. A.; Marchese, A. J.; Hamburg, S. P. Concurrent Variation in Oil and Gas Methane Emissions and Oil Price during the COVID-19 Pandemic. *Atmos. Chem. Phys.* **2021**, *21*, 6605−6626.

(7) Zhang, Y.; Gautam, R.; Pandey, S.; Omara, M.; Maasakkers, J. D.; Sadavarte, P.; Lyon, D.; Nesser, H.; Sulprizio, M. P.; Varon, D. J.; Zhang, R.; Houweling, S.; Zavala-Araiza, D.; Alvarez, R. A.; Lorente, A.; Hamburg, S. P.; Aben, I.; Jacob, D. J. Quantifying Methane Emissions from the Largest Oil-Producing Basin in the United States from Space. *Sci. Adv.* **2020**, *6*, No. eaaz5120.

(8) Lin, J. C.; Bares, R.; Fasoli, B.; Garcia, M.; Crosman, E.; Lyman, S. Declining Methane Emissions and Steady, High Leakage Rates Observed over Multiple Years in a Western US Oil/Gas Production Basin. *Sci. Rep.* **2021**, *11*, 22291.

(9) Rutherford, J. S.; Sherwin, E. D.; Ravikumar, A. P.; Heath, G. A.; Englander, J.; Cooley, D.; Lyon, D.; Omara, M.; Langfitt, Q.; Brandt, A. R. Closing the Methane Gap in US Oil and Natural Gas Production Emissions Inventories. *Nat. Commun.* **2021**, *12*, 4715.
(10) Ahmadov, R.; McKeen, S. A.; Trainer, M.; Banta, R. M.; Brewer, A.; Brown, S. S.; Edwards, P. M.; de Gouw, J. A.; Frost, G. J.; Gilman, J. B.; Helmig, D.; Johnson, B.; Karion, A.; Koss, A. R.; Langford, A.; Lerner, B. M.; Olson, J.; Oltmans, S.; Peischl, J.; Petron, G.; Pichugina, Y.; Roberts, J. M.; Ryerson, T.; Schnell, R. C.; Senff, C.; Sweeney, C.; Thompson, C.; Veres, P.; Warneke, C.; Wild, R.; Williams, E. J.; Yuan, B.; Zamora, R. Understanding High Wintertime Ozone Pollution Events in an Oil and Natural Gas-Producing Region of the Western US. *Atmos. Chem. Phys.* **2015**, *15*, 411−429.
(11) Edwards, P. M.; Brown, S. S.; Roberts, J. M.; Ahmadov, R.; Banta, R. M.; de Gouw, J. A.; Dubé, W. P.; Field, R. A.; Flynn, J. H.; Gilman, J. B.; Graus, M.; Helmig, D.; Koss, A. R.; Langford, A. O.; Lefer, B. L.; Lerner, B. M.; Li, R.; Li, S.-M.; McKeen, S. A.; Murphy, S. M.; Parrish, D. D.; Senff, C. J.; Soltis, J.; Stutz, J.; Sweeney, C.; Thompson, C. R.; Trainer, M. K.; Tsai, C.; Veres, P. R.; Washenfelder, R. A.; Warneke, C.; Wild, R. J.; Young, C. J.; Yuan, B.; Zamora, R. High Winter Ozone Pollution from Carbonyl Photolysis in an Oil and Gas Basin. *Nature* **2014**, *514*, 351−354.
(12) Duncan, B. N.; Lamsal, L. N.; Thompson, A. M.; Yoshida, Y.; Lu, Z.; Streets, D. G.; Hurwitz, M. M.; Pickering, K. E. A Space-Based, High-Resolution View of Notable Changes in Urban NO_x Pollution around the World (2005-2014). *J. Geophys. Res.: Atmos.* **2016**, *121*, 976−996.
(13) Majid, A.; Martin, M. V.; Lamsal, L. N.; Duncan, B. N. A Decade of Changes in Nitrogen Oxides over Regions of Oil and Natural Gas Activity in the United States. *Elementa-Sci. Anthrop.* **2017**, *5*, 76.
(14) Dix, B.; de Bruin, J.; Roosenbrand, E.; Vlemmix, T.; Francoeur, C.; Gorchov-Negron, A.; McDonald, B.; Zhizhin, M.; Elvidge, C.; Veefkind, P.; Levelt, P.; de Gouw, J. Nitrogen Oxide Emissions from U.S. Oil and Gas Production: Recent Trends and Source Attribution. *Geophys. Res. Lett.* **2020**, *47*, No. e2019GL085866.
(15) Beirle, S.; Borger, C.; Dörner, S.; Li, A.; Hu, Z.; Liu, F.; Wang, Y.; Wagner, T. Pinpointing Nitrogen Oxide Emissions from Space. *Sci. Adv.* **2019**, *5*, No. eaax9800.
(16) Beirle, S.; Borger, C.; Dörner, S.; Eskes, H.; Kumar, V.; de Laat, A.; Wagner, T. Catalog of NO_x Emissions from Point Sources as Derived from the Divergence of the NO_2 Flux for TROPOMI. *Earth Syst. Sci. Data* **2021**, *13*, 2995−3012.
(17) Gorchov Negron, A. M.; McDonald, B. C.; McKeen, S. A.; Peischl, J.; Ahmadov, R.; de Gouw, J. A.; Frost, G. J.; Hastings, M. G.; Pollack, I. B.; Ryerson, T. B.; Thompson, C.; Warneke, C.; Trainer, M. Development of a Fuel-Based Oil and Gas Inventory of Nitrogen Oxides Emissions. *Environ. Sci. Technol.* **2018**, *52*, 10175−10185.
(18) Liu, M.; van der A, R.; van Weele, M.; Eskes, H.; Lu, X.; Veefkind, P.; de Laat, J.; Kong, H.; Wang, J.; Sun, J.; Ding, J.; Zhao, Y.; Weng, H. A New Divergence Method to Quantify Methane Emissions Using Observations of Sentinel-5P TROPOMI. *Geophys. Res. Lett.* **2021**, *48*, No. e2021GL094151.
(19) Lin, J.-T.; McElroy, M. B.; Boersma, K. F. Constraint of Anthropogenic NO_x Emissions in China from Different Sectors: A New Methodology Using Multiple Satellite Retrievals. *Atmos. Chem. Phys.* **2010**, *10*, 63−78.
(20) Beirle, S.; Boersma, K. F.; Platt, U.; Lawrence, M.; Wagner, T. Megacity Emissions and Lifetimes of Nitrogen Oxides Probed from Space. *Science* **2011**, *333*, 1737−1739.
(21) Duncan, B. N.; Yoshida, Y.; de Foy, B.; Lamsal, L. N.; Streets, D. G.; Lu, Z.; Pickering, K. E.; Krotkov, N. A. The Observed Response of Ozone Monitoring Instrument (OMI) NO_2 Columns to NO_x Emission Controls on Power Plants in the United States: 2005−2011. *Atmos. Environ.* **2013**, *81*, 102−111.
(22) Liu, F.; Beirle, S.; Zhang, Q.; Dörner, S.; He, K.; Wagner, T. NO_x Lifetimes and Emissions of Cities and Power Plants in Polluted Background Estimated by Satellite Observations. *Atmos. Chem. Phys.* **2016**, *16*, 5283−5298.
(23) Laughner, J. L.; Cohen, R. C. Quantification of the Effect of Modeled Lightning NO_2 on UV−Visible Air Mass Factors. *Atmos. Meas. Tech.* **2017**, *10*, 4403−4419.
(24) Nault, B. A.; Laughner, J. L.; Wooldridge, P. J.; Crounse, J. D.; Dibb, J.; Diskin, G.; Peischl, J.; Podolske, J. R.; Pollack, I. B.; Ryerson, T. B.; Scheuer, E.; Wennberg, P. O.; Cohen, R. C. Lightning NO_x Emissions: Reconciling Measured and Modeled Estimates With Updated NO_x Chemistry. *Geophys. Res. Lett.* **2017**, *44*, 9479−9488.
(25) Goldberg, D. L.; Lu, Z.; Streets, D. G.; de Foy, B.; Griffin, D.; McLinden, C. A.; Lamsal, L. N.; Krotkov, N. A.; Eskes, H. Enhanced Capabilities of TROPOMI NO_2: Estimating NO_x from North American Cities and Power Plants. *Environ. Sci. Technol.* **2019**, *53*, 12594−12601.
(26) Lorente, A.; Boersma, K. F.; Eskes, H. J.; Veefkind, J. P.; van Geffen, J. H. G. M.; de Zeeuw, M. B.; Denier van der Gon, H. A. C.; Beirle, S.; Krol, M. C. Quantification of Nitrogen Oxides Emissions from Build-up of Pollution over Paris with TROPOMI. *Sci. Rep.* **2019**, *9*, 20033.
(27) Veefkind, J. P.; Aben, I.; McMullan, K.; Förster, H.; de Vries, J.; Otter, G.; Claas, J.; Eskes, H. J.; de Haan, J. F.; Kleipool, Q.; van Weele, M.; Hasekamp, O.; Hoogeveen, R.; Landgraf, J.; Snel, R.; Tol, P.; Ingmann, P.; Voors, R.; Kruizinga, B.; Vink, R.; Visser, H.; Levelt, P. F. TROPOMI on the ESA Sentinel-5 Precursor: A GMES Mission for Global Observations of the Atmospheric Composition for Climate, Air Quality and Ozone Layer Applications. *Remote Sens. Environ.* **2012**, *120*, 70−83.
(28) van Geffen, J. H. G. M.; Boersma, K. F.; Van Roozendael, M.; Hendrick, F.; Mahieu, E.; De Smedt, I.; Sneep, M.; Veefkind, J. P. Improved Spectral Fitting of Nitrogen Dioxide from OMI in the 405−465 Nm Window. *Atmos. Meas. Tech.* **2015**, *8*, 1685−1699.
(29) van Geffen, J. H. G. M.; Eskes, H.; Boersma, K. F.; Veefkind, J. P. *TROPOMI ATBD of the Total and Tropospheric NO_2 Data Products*; S5P-KNMI-L2−0005-RP; 2021; p 86.
(30) Hoffmann, L.; Günther, G.; Li, D.; Stein, O.; Wu, X.; Griessbach, S.; Heng, Y.; Konopka, P.; Müller, R.; Vogel, B.; Wright, J. S. From ERA-Interim to ERA5: The Considerable Impact of ECMWF's next-Generation Reanalysis on Lagrangian Transport Simulations. *Atmos. Chem. Phys.* **2019**, *19*, 3097−3124.
(31) McDonald, B. C.; McBride, Z. C.; Martin, E. W.; Harley, R. A. High-Resolution Mapping of Motor Vehicle Carbon Dioxide Emissions. *J. Geophys. Res.-Atmos.* **2014**, *119*, 5283−5298.
(32) McDonald, B. C.; McKeen, S. A.; Cui, Y. Y.; Ahmadov, R.; Kim, S.-W.; Frost, G. J.; Pollack, I. B.; Peischl, J.; Ryerson, T. B.; Holloway, J.; Graus, M. G.; Warneke, C.; Gilman, J. B.; de Gouw, J. A.; Kaiser, J. B.; Keutsch, F. N.; Hanisco, T. F.; Wolfe, G. M.; Trainer, M. Modeling Ozone in the Eastern U.S. Using a Fuel-Based Mobile Source Emissions Inventory. *Environ. Sci. Technol.* **2018**, *52*, 7360−7370.
(33) Jenkin, M. E.; Saunders, S. M.; Wagner, V.; Pilling, M. J. Protocol for the Development of the Master Chemical Mechanism, MCM v3 (Part B): Tropospheric Degradation of Aromatic Volatile Organic Compounds. *Atmos. Chem. Phys.* **2003**, *3*, 181−193.
(34) Saunders, S. M.; Jenkin, M. E.; Derwent, R. G.; Pilling, M. J. Protocol for the Development of the Master Chemical Mechanism, MCM v3 (Part A): Tropospheric Degradation of Non-Aromatic Volatile Organic Compounds. *Atmos. Chem. Phys.* **2003**, *3*, 161−180.
(35) Rohrer, F.; Berresheim, H. Strong Correlation between Levels of Tropospheric Hydroxyl Radicals and Solar Ultraviolet Radiation. *Nature* **2006**, *442*, 184−187.
(36) Jenkin, M. E.; Saunders, S. M.; Pilling, M. J. The Tropospheric Degradation of Volatile Organic Compounds: A Protocol for Mechanism Development. *Atmos. Environ.* **1997**, *31*, 81−104.
(37) U.S. Field Production of Crude Oil (Thousand Barrels per Day) https://www.eia.gov/dnav/pet/hist/LeafHandler.ashx?n=pet&s=mcrfpus2&f=m (accessed 2021−10 -25).
(38) U.S. Natural Gas Gross Withdrawals (Million Cubic Feet) https://www.eia.gov/dnav/ng/hist/n9010us2m.htm (accessed 2021−10 -25).

https://doi.org/10.1021/acsearthspacechem.1c00387
ACS Earth Space Chem. 2022, 6, 403−414

(39) Drilling Productivity Report - U.S. Energy Information Administration (EIA) https://www.eia.gov/petroleum/drilling/index.php (accessed 2021−10 -25).
(40) Verhoelst, T.; Compernolle, S.; Pinardi, G.; Lambert, J.-C.; Eskes, H. J.; Eichmann, K.-U.; Fjæraa, A. M.; Granville, J.; Niemeijer, S.; Cede, A.; Tiefengraber, M.; Hendrick, F.; Pazmiño, A.; Bais, A.; Bazureau, A.; Boersma, K. F.; Bognar, K.; Dehn, A.; Donner, S.; Elokhov, A.; Gebetsberger, M.; Goutail, F.; Grutter de la Mora, M.; Gruzdev, A.; Gratsea, M.; Hansen, G. H.; Irie, H.; Jepsen, N.; Kanaya, Y.; Karagkiozidis, D.; Kivi, R.; Kreher, K.; Levelt, P. F.; Liu, C.; Müller, M.; Navarro Comas, M.; Piters, A. J. M.; Pommereau, J.-P.; Portafaix, T.; Prados-Roman, C.; Puentedura, O.; Querel, R.; Remmers, J.; Richter, A.; Rimmer, J.; Rivera Cárdenas, C.; Saavedra de Miguel, L.; Sinyakov, V. P.; Stremme, W.; Strong, K.; Van Roozendael, M.; Veefkind, J. P.; Wagner, T.; Wittrock, F.; Yela González, M.; Zehner, C. Ground-Based Validation of the Copernicus Sentinel-5P TROPOMI NO_2 Measurements with the NDACC ZSL-DOAS, MAX-DOAS and Pandonia Global Networks. *Atmos. Meas. Tech.* **2021**, *14*, 481−510.
(41) de Gouw, J. A.; Veefkind, J. P.; Roosenbrand, E.; Dix, B.; Lin, J. C.; Landgraf, J.; Levelt, P. F. Daily Satellite Observations of Methane from Oil and Gas Production Regions in the United States. *Sci. Rep.* **2020**, *10*, 1379.

https://doi.org/10.1021/acsearthspacechem.1c00387
ACS Earth Space Chem. 2022, 6, 403−414